

1 Effects of high-energy particle showers on the embedded
2 front-end electronics of an electromagnetic calorimeter for a
3 future lepton collider

4 **The CALICE Collaboration**

5 **Abstract**

6 Application Specific Integrated Circuits, ASICs, similar to those envisaged for the
7 readout electronics of the central calorimeters of detectors for a future lepton collider
8 have been exposed to high-energy electromagnetic showers. A salient feature of these
9 calorimeters is that the readout electronics will be embedded into the calorimeter layers.
10 In this article it is shown that interactions of shower particles in the volume of the readout
11 electronics do not alter the noise pattern of the ASICs. No signal at or above the MIP
12 level has been observed during the exposure. The upper limit at the 95% confidence level
13 on the frequency of fake signals is smaller than $1 \cdot 10^{-5}$ for a noise threshold of about 60%
14 of a MIP. For ASICs with similar design to those which were tested, it can thus be largely
15 excluded that the embedding of the electronics into the calorimeter layers compromises
16 the performance of the calorimeters.

17 *Keywords: Lepton collider; electromagnetic calorimeter; embedded electronics; fake hits*

18 C. Adloff
19 *Laboratoire d'Annecy-le-Vieux de Physique des Particules, Université de Savoie, CNRS/IN2P3, 9 Chemin de*
20 *Bellevue BP110, F-74941 Annecy-le-Vieux CEDEX, France*

21 K. Francis, J. Repond, J. Smith^{*}, D. Trojand[†], L. Xia
22 *Argonne National Laboratory, 9700 S. Cass Avenue, Argonne, IL 60439-4815, USA*

23 E. Baldolemar, J. Li[‡], S. T. Park, M. Sosebee, A. P. White, J. Yu
24 *Department of Physics, SH108, University of Texas, Arlington, TX 76019, USA*

25 Y. Mikami, N. K. Watson
26 *University of Birmingham, School of Physics and Astronomy, Edgbaston, Birmingham B15 2TT, UK*

27 G. Mavromanolakis[§], M. A. Thomson, D. R. Ward, W. Yan[¶]
28 *University of Cambridge, Cavendish Laboratory, J J Thomson Avenue, CB3 0HE, UK*

29 D. Bencheekroun, A. Hoummada, Y. Khoulaki
30 *Réseau Universitaire de Physique des Hautes Energies (RUPHE), Université Hassan II Aïn Chock, Faculté*
31 *des sciences. B.P. 5366 Maarif, Casablanca, Morocco*

32 M. Benyamna, C. Cârloganu, F. Fehr, P. Gay, S. Manen, L. Royer
33 *Clermont Université, Université Blaise Pascal, CNRS/IN2P3, LPC, BP 10448, F-63000 Clermont-Ferrand,*
34 *France*

35 G. C. Blazey, A. Dyshkant, V. Zutshi
36 *NICADD, Northern Illinois University, Department of Physics, DeKalb, IL 60115, USA*

37 J. -Y. Hostachy, L. Morin
38 *Laboratoire de Physique Subatomique et de Cosmologie - Université Joseph Fourier Grenoble 1 -*
39 *CNRS/IN2P3 - Institut Polytechnique de Grenoble, 53, rue des Martyrs, 38026 Grenoble CEDEX, France*

40 U. Cornett, D. David, R. Fabbri, G. Falley, K. Gadow, E. Garutti, P. Göttlicher, C. Günter,
41 S. Karstensen, F. Krivan, A. -I. Lucaci-Timoce[§], S. Lu, B. Lutz, I. Marchesini, N. Meyer,
42 S. Morozov, V. Morgunov^{||}, M. Reinecke, F. Sefkow, P. Smirnov, M. Terwort,
43 A. Vargas-Trevino, N. Wattimena, O. Wendt
44 *DESY, Notkestrasse 85, D-22603 Hamburg, Germany*

45 N. Feege, J. Haller, S. Richter, J. Samson
46 *Univ. Hamburg, Physics Department, Institut für Experimentalphysik, Luruper Chaussee 149, 22761*
47 *Hamburg, Germany*

48 P. Eckert, A. Kaplan, H. -Ch. Schultz-Coulon, W. Shen, R. Stamen, A. Tadday
49 *University of Heidelberg, Fakultät für Physik und Astronomie, Albert-Ueberle Str. 3-5 2.OG Ost, D-69120*
50 *Heidelberg, Germany*

51 B. Bilki, E. Norbeck, Y. Onel
52 *University of Iowa, Dept. of Physics and Astronomy, 203 Van Allen Hall, Iowa City, IA 52242-1479, USA*

53 K. Kawagoe, S. Uozumi^{**}
54 *Department of Physics, Kobe University, Kobe, 657-8501, Japan*

55 P. D. Dauncey, A. -M. Magnan

56 *Imperial College London, Blackett Laboratory, Department of Physics, Prince Consort Road, London SW7*
57 *2AZ, UK*

58 *V. Bartsch^{††}*
59 *Department of Physics and Astronomy, University College London, Gower Street, London WC1E 6BT, UK*

60 *F. Salvatore^{††}*
61 *Royal Holloway University of London, Dept. of Physics, Egham, Surrey TW20 0EX, UK*

62 *I. Laktineh*
63 *Université de Lyon, Université de Lyon 1, CNRS/IN2P3, IPNL 4 rue E Fermi 69622, Villeurbanne*
64 *CEDEX, France*

65 *E. Calvo Alamillo, M.-C. Fouz, J. Puerta-Pelayo*
66 *CIEMAT, Centro de Investigaciones Energeticas, Medioambientales y Tecnologicas, Madrid, Spain*

67 *A. Frey^{†‡}, C. Kiesling, F. Simon*
68 *Max Planck Inst. für Physik, Föhringer Ring 6, D-80805 Munich, Germany*

69 *J. Bonis, B. Bouquet, S. Callier, P. Corneise, Ph. Doublet, F. Dulucq, M. Faucci Giannelli,*
70 *J. Fleury, H. Li[♣], G. Martin-Chassard, F. Richard, Ch. de la Taille, R. Pöschl, L. Raux,*
71 *N. Seguin-Moreau, F. Wicek*
72 *Laboratoire de l'Accélérateur Linéaire, Centre Scientifique d'Orsay, Université de Paris-Sud XI,*
73 *CNRS/IN2P3, BP 34, Bâtiment 200, F-91898 Orsay Cedex, France*

74 *M. Anduze, V. Boudry, J-C. Brient, D. Jeans, P. Mora de Freitas, G. Musat, M. Reinhard,*
75 *M. Ruan, H. Videau*
76 *Laboratoire Leprince-Ringuet (LLR) – École Polytechnique, CNRS/IN2P3, F-91128 Palaiseau, France*

77 *M. Marcisovsky, P. Sicho, V. Vrba, J. Zalesak*
78 *Institute of Physics, Academy of Sciences of the Czech Republic, Na Slovance 2, CZ-18221 Prague 8, Czech*
79 *Republic*

80 *B. Belhorma, H. Ghazlane*
81 *Centre National de l'Energie, des Sciences et des Techniques Nucléaires, B.P. 1382, R.P. 10001, Rabat,*
82 *Morocco*

84 ** Also at University of Texas, Arlington*
85

86 *† Also at McGill University, Department of Physics, 3600 University Street, Montréal, Québec, Canada,*
87 *H3A 2T8*

88 *‡ Deceased*

89 *§ Now at CERN*

90 *¶ Now at Dept. of Modern Physics, Univ. of Science and Technology of China, 96 Jinzhai Road, Hefei,*
91 *Anhui, 230026, P. R. China*

92 *|| On leave from ITEP*

93 *** Now at Kyungpook Nation University, 1370 Sankyuk-dong, Buk-go Daegu 701-701, Korea*

94 ^{††}Now at University of Sussex, Physics and Astronomy Department, Brighton, Sussex, BN1 9QH, UK

95 ^{‡‡}Now at University of Göttingen, II. Physikalisches Institut Friedrich-Hund-Platz 1, 37077 Göttingen,
96 Germany

97 [♣]Now at LPSC Grenoble

98 **1 Introduction**

99 The central calorimeters of the detectors to be operated at a future lepton collider will have
 100 the readout electronics embedded into the active layers of the calorimeter [1, 2, 3]. The
 101 energy of electromagnetic showers produced in the final states ranges between a few MeV
 102 up to several hundreds of GeV. A natural question arising from this design is whether the
 103 cascade particles of the high-energy showers which penetrate through the electronics do create
 104 radiation induced effects in these circuits. These effects would compromise the precision
 105 measurements envisaged at the lepton collider. Possible radiation effects include Transient
 106 Effects and Single Event Upsets [4] which may create pulses which would be recorded as *fake*
 107 *signals* or, even worse, could cause damage to the readout electronics.

108 The CALICE collaboration is designing, building and operating large scale prototypes for
 109 the calorimeters at a future lepton collider [5]. Large statistics data samples have been
 110 recorded in test beam campaigns in order to understand the behaviour of highly granular
 111 calorimeters. This article describes the measurements conducted in a special set of runs in
 112 which an ordinary calorimeter layer of a prototype for a silicon tungsten electromagnetic
 113 calorimeter, called *SiW Ecal* hereafter, has been replaced by a *special PCB* allowing for the
 114 exposure of the readout electronics to particle showers. The data analysed here were recorded
 115 during the 2007 test beam campaign at CERN in the H6 test beam area

116 **2 Experimental set-up and data taking**

117 Figure 1 shows a perspective view on the *physics prototype* of the SiW Ecal. A comprehensive
 118 description of the physics prototype is given elsewhere [6]. Here only those features relevant
 119 for the present analysis will be outlined.

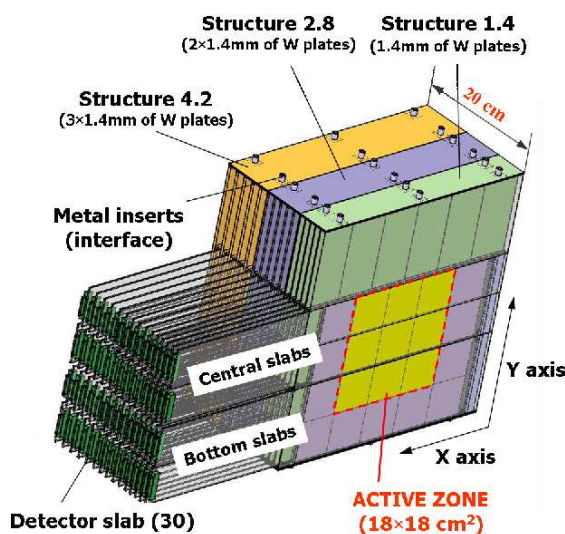


Figure 1: Schematic 3D view of the physics prototype.

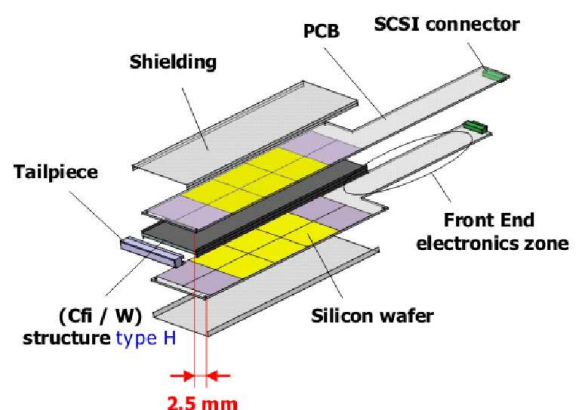


Figure 2: Schematic diagram showing the components of a detector slab.

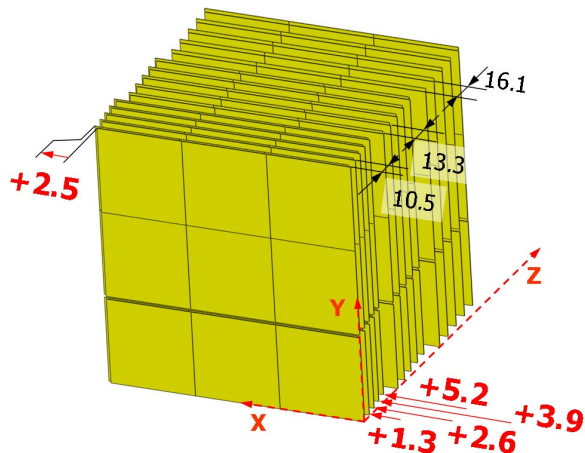


Figure 3: Illustration of layer offsets (2.5 mm) and slabs offsets (1.3 mm) of the physics prototype of the SiW Ecal as discussed in the text. Shown is also the total extension of the three modules in z -direction. All dimensions are in mm.

120 The physics prototype consists of 9720 $1 \times 1 \text{ cm}^2$ wide calorimeter cells subdivided into 30
 121 layers. The active zone covers $18 \times 18 \text{ cm}^2$ in width and approximately 20 cm in depth. The
 122 layers are composed alternately by W absorber plates and a matrix of PIN diode sensors
 123 on a silicon wafer substrate. At normal incidence, the prototype has a total depth of $24 X_0$
 124 achieved using 10 layers of $0.4 X_0$ tungsten absorber plates, followed by 10 layers of $0.8 X_0$,
 125 and another 10 layers of $1.2 X_0$ thick plates. Each layer is subdivided into a central part
 126 featuring a 3×2 array of silicon wafers and a bottom part consisting of a 3×1 array of silicon
 127 wafers. Note that in the running period relevant for this analysis the bottom part of the first
 128 six layers was missing.

129 The silicon wafers are mounted onto both sides of an H-shaped tungsten plate as shown in
 130 Figure 2. Such an entity is called a *slab*. In order to avoid an alignment of wafer boundaries,
 131 the layers within a slab are shifted by 2.5 mm in the positive x -direction with respect to each
 132 other. In the same way, two successive slabs are shifted by 1.3 mm with respect to each other.
 133 The layer offsets are illustrated in Figure 3.

134 As indicated in Figures 1 and 2, the readout electronics are located outside the absorber
 135 structure and hence not exposed to high-energy electromagnetic showers. The main device
 136 of the read out electronics is an 18 channel charge sensitive ASIC, called FLC_PHY3 which
 137 is realised in $0.8 \mu\text{m}$ AMS BiCMOS technology. One 6×6 sensor matrix is thus read out
 138 by two ASICs. This provides redundancy by de-correlating ASIC and sensor response. As
 139 shown in Figure 4, the signal path starts with a variable gain charge preamplifier, followed
 140 by two shaping filters for gains 1 and 10 with a shaping time of 180 ns for both gains. The
 141 shaped signal is then propagated to a sample and hold device realised by a 2 pF capacitance.
 142 After that the measured voltage, which is proportional to the charge at the input of the

143 pre-amplifier, is written into a buffer designed to store the 18 signals as processed by the
 144 signal chain. The 18 signals are read one-by-one by the off-detector electronics. One channel
 145 covers a dynamic range equivalent to the energy deposition by about 600 *Minimum Ionising*
 146 *Particles*, MIPs, which has been considered to be sufficient for a beam test using primary
 147 electrons of an energy of up to 50 GeV.

148 For the present tests, FLC_PHY3 ASICs were exposed to electromagnetic showers. One ASIC
 149 has a surface of about $1.6 \times 2.3 \text{ mm}^2$. It is TQFP64 packaged such that the whole ensemble
 150 has outer dimensions of about $1 \times 1 \text{ cm}^2$ [7]. The shower particles may create charges and
 151 thus fake signals in the PMOS at the entrance of the pre-amplifiers of the 18 channels. The
 152 sensitive area of one channel is about $3000 \mu\text{m}^2$ while the total surface of a channel is about
 153 $110000 \mu\text{m}^2$. Signals created in the circuitry after the pre-amplifier which would appear
 154 immediately at the output of the ASIC cannot be recorded due to the sampling latency of
 155 180 ns of the CALICE data acquisition system. Radiation effects could therefore only become
 156 apparent in case of a failure of the circuitry. Such a failure has not been observed during the
 157 tests presented in this article.

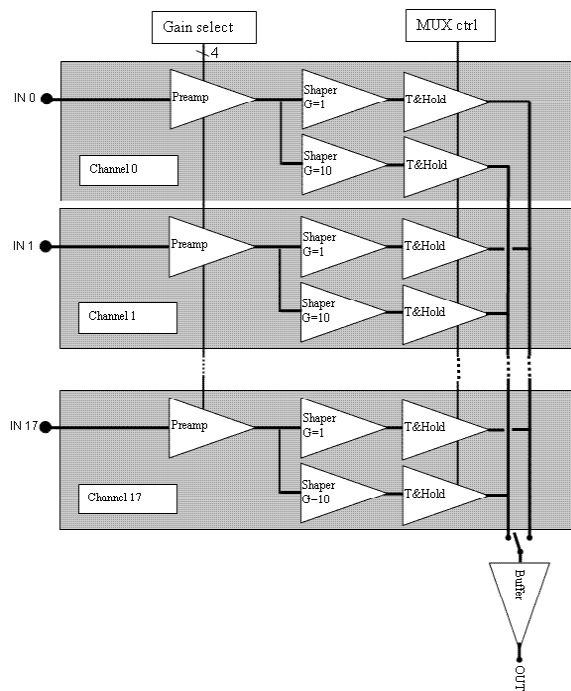


Figure 4: *General block schematic of FLC_PHY3.*

158 The special PCB is equipped with four ASICs in the nominal sensitive plane of the detector.
 159 It has been mounted directly on a spare H-board as shown in Figure 5. The special PCB has
 160 been placed within the physics prototype at the layer corresponding to the expected position
 161 of the shower maximum. In this configuration data with electrons with an energy of 70 GeV
 162 and 90 GeV have been recorded. The lateral spread of the electron beam at these energies
 163 is about 1 cm in diameter [6]. The beam has been positioned at five different points along
 164 the x -direction at the centre in y of each of the four ASICs as indicated for the 'ASIC 1' in
 165 Figure 6. Beam events triggered with scintillation counters, called *signal events* hereafter, are
 166 interleaved during the data taking with *pedestal events* triggered by an oscillator integrated

167 into the CALICE data acquisition system. For further details of the experimental set-up
168 please consult [6, 8, 9]. Table 1 gives the number of recorded signal and pedestal events
169 at each measurement point. The table also introduces the nomenclature used hereafter to
170 identify the various measurement points.

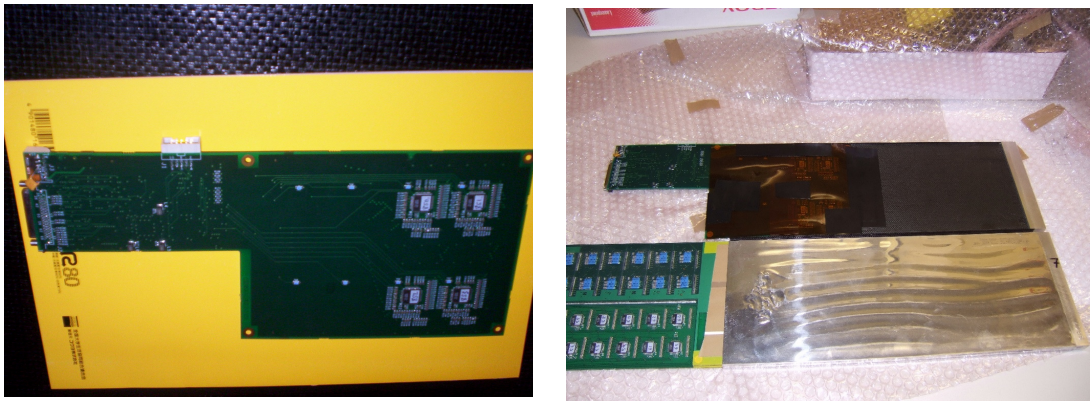


Figure 5: *Left: Picture of the special PCB with the four ASICs used in the test. Right: The special PCB mounted on tungsten absorber and comparison with a regular slab.*

171 **3 Initial steps of data analysis**

172 The data are verified for a proper alignment of the ASICs relative to the beam in lateral
173 direction and to the shower maximum in longitudinal direction. Figure 7 shows the spectra
174 of a run with electrons of 90 GeV. Here, the recorded data were reconstructed with the same
175 reconstruction chain as applied to the regular data taking [6, 8]. The energy deposition in
176 the detector is given in terms of MIPs and 1 MIP corresponds to about 45 *ADC counts* [6]
177 as recorded by the CALICE data acquisition system. The reconstruction chain introduces a
178 zero suppression at 0.6 MIP corresponding to approximately 4.5 times the mean noise level
179 of 6 ADC counts. In addition, a correction for pedestal instabilities caused by insufficient
180 isolation of the power supply lines of the PCBs is applied [6]. After this correction the residual
181 pedestal instability is about 0.2% of a MIP (or 0.1 ADC counts).

182 The total energy spectrum exhibits a clear maximum well separated from residual noise and
183 MIP events. The gap visible in the longitudinal shower profile indicates that the special

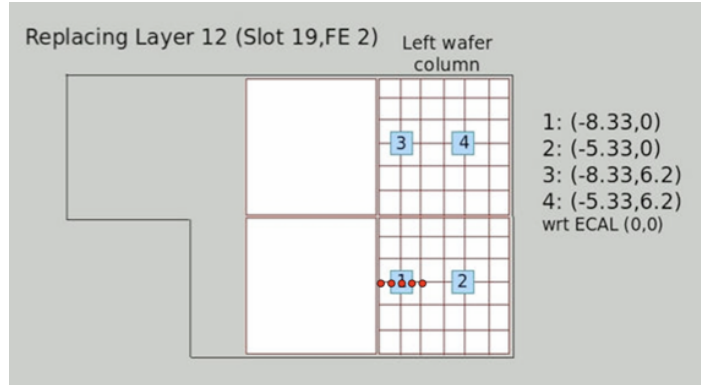


Figure 6: Schematic view of the special PCB. The red points indicate the nominal five impact points for a scan over ASIC 1. Identical scans have been performed for the other three ASICs.

184 layer has been placed close to the shower maximum. The lateral position of the special PCB,
 185 installed at the position of Layer 12, is identical to that of the Layer 2 of the prototype. As
 186 an example, Figure 8 shows the hit maps of layers 2 and 14 for a run in which the beam was
 187 incident on ASIC 4. The Layer 14 is the first regular layer behind the special PCB. Overlaid
 188 to the hit maps is the projected position of ASIC 4. The gaps in the lower parts of the hit
 189 maps can be explained by non-instrumented parts of the detector.

190 It is clearly visible that the beam hits the detector close to the ASIC position and that
 191 the lateral shower development leads to a good coverage and thus good exposure to shower
 192 particles of the ASIC.

193 In a next step the regular zero suppression was switched off in the CALICE reconstruction
 194 program in order to be sensitive to the behaviour of the ASICs in the small signal range. For
 195 technical reasons the first channel of each ASIC on the special PCB is discarded, leaving 17
 196 signals per ASIC per event. As motivated by the energy spectrum shown in Figure 7, the
 197 signal events are further selected by requiring an energy deposition of more than 2000 MIPs
 198 in order to be unbiased by MIP-like events. This cut reduces the available statistics quoted
 199 in Table 1 by approximately 15%. Still, no difference between the noise spectra obtained
 200 for signal and pedestal events is expected. As an example, in Figure 9 the noise spectra
 201 of signal and pedestal events are compared the Measurement point 3 of Scan 4. Indeed,
 202 no difference between the two data types can be observed. After this initial qualitative
 203 comparison, the mean and the root mean square (RMS) for each ASIC at each measurement
 204 point are extracted for signal and pedestal events. The results are displayed in Figure 10,
 205 using the scan over ASIC 1 as an example.

206 The corresponding figures for the other scans are given in the appendix. From these figures
 207 the following conclusions can be drawn:

- 208 • The mean and the RMS remain the same throughout all the runs. In particular no
 209 dependence on the scan position can be observed.
- 210 • The mean and RMS for signal and pedestal events are always nearly identical. Residual

Scan	Beam centred on	Measurement point	Position: x,y [cm]	Signal events	Pedestal events
1	ASIC 1	1	-9.33, 0	78293	14624
		2	-8.83, 0	189966	37173
		3	-8.33, 0	209312	38361
		4	-7.83, 0	65249	3602
		5	-7.33, 0	85543	4306
2	ASIC 2	1	-6.33, 0	85188	4678
		2	-5.83, 0	129778	6146
		3	-5.33, 0	213369	13719
		4	-4.83, 0	217111	11053
		5	-4.33, 0	89435	4254
3	ASIC 3	1	-9.33, 6.2	90395	4347
		2	-8.83, 6.2	228138	10296
		3	-8.33, 6.2	216877	9831
		4	-7.83, 6.2	218519	9462
		5	-7.33, 6.2	86989	3909
4	ASIC 4	1	-6.33, 6.2	66655	4223
		2	-5.83, 6.2	214418	13666
		3	-5.33, 6.2	314275	15264
		4	-4.83, 6.2	217415	11698
		5	-4.33, 6.2	85884	4949

Table 1: Protocol of the exposure test containing the identifiers of the measurement points, their position and the number of signal and pedestal events recorded at each position.

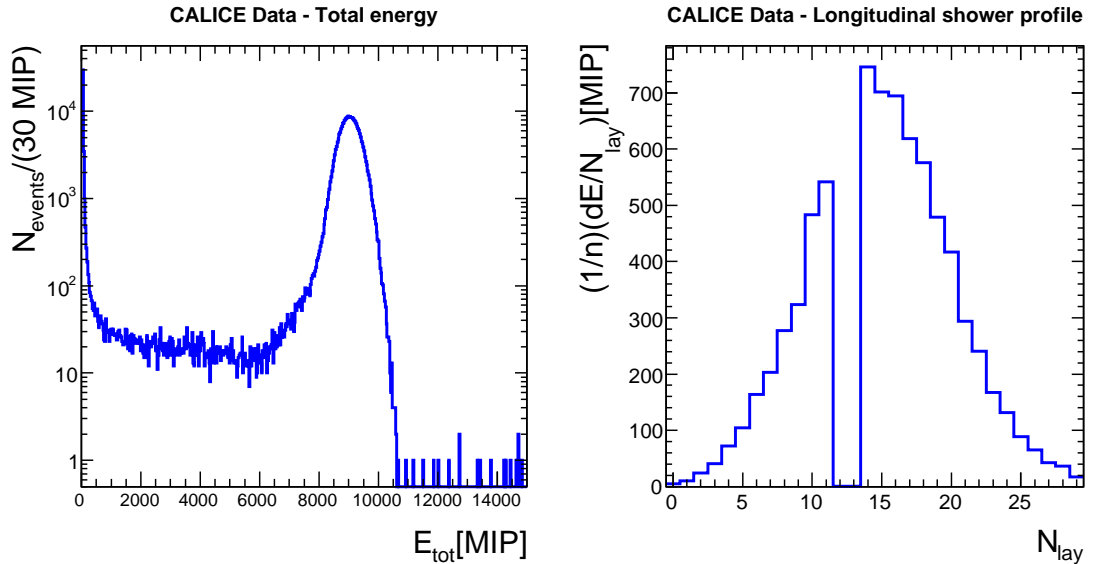


Figure 7: Total energy deposition and longitudinal shower profile for a run with electrons of 90 GeV during the test with the special PCB. The gap visible in the longitudinal shower profile is due to the replacement of a regular slab by the H-board carrying the special PCB.

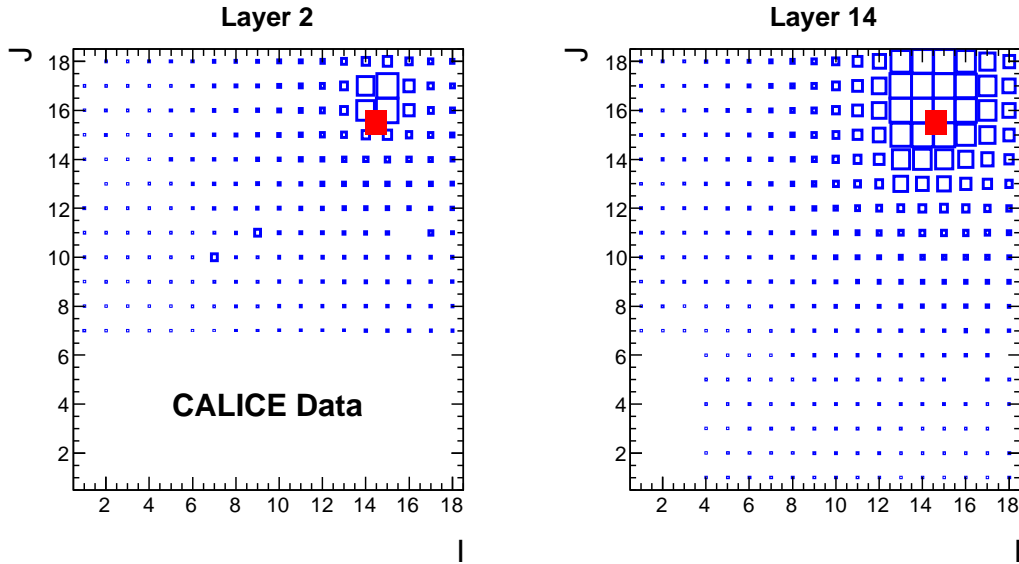


Figure 8: Hit maps shown as a function of the cell indices I , J in x and y -directions in layer 2 and 14. The area of the boxes represents the number of recorded hits in the individual cells. The position of ASIC 4, indicated by the full square, is projected into the planes of these layers.

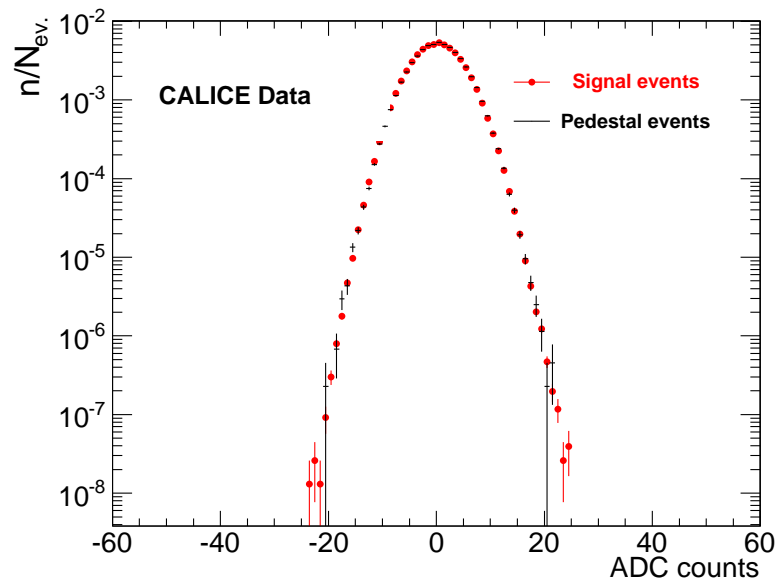


Figure 9: Noise spectrum for signal events and pedestal events. The figure displays the result for the run in which the beam was centred on ASIC 4. The distributions are normalised to unity.

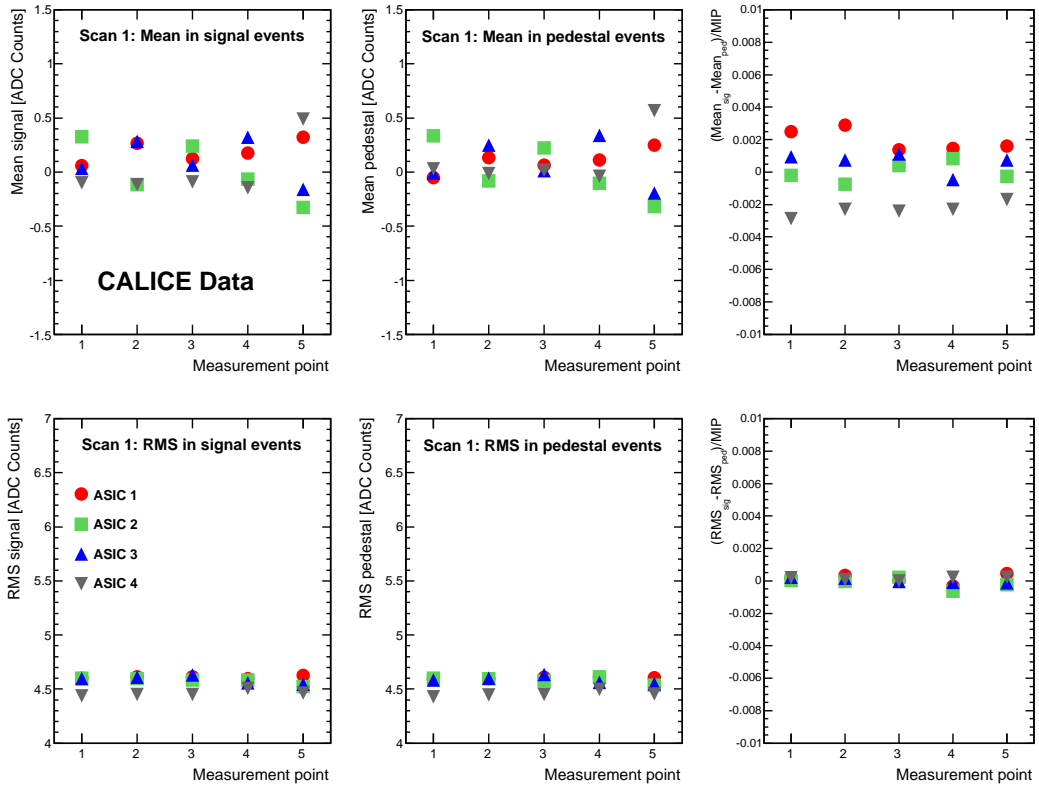


Figure 10: Mean and RMS for signal events and pedestal events. The very right part shows the corresponding differences normalised to the value of a MIP assumed to be 45 ADC counts. The figure displays the result for Scan 1 in which ASIC 1 is scanned. As a cross-check the results for all ASICs are shown.

211 differences are smaller than 0.4% of a MIP.

212 4 Detailed noise analysis

213 The high-energy showers penetrating the electronics may disturb the noise characteristics
 214 of the exposed ASICs. This perturbation may be revealed in changes of the coherent and
 215 incoherent noise levels of the ASICs. A very robust and widely used technique to analyse noise
 216 patterns in data is given by a *Principal Component Analysis (PCA)*. The analysis performed
 217 in this paper follows that presented in [10]. As was pointed out there and confirmed in present
 218 study, the PCA leads to more reliable results than a more simplistic approach based on direct
 219 and alternating sums.

220 **4.1 Principal Component Analysis - PCA**

221 The PCA can be subdivided into five steps which are introduced now. Each step will be
 222 illustrated by the results obtained for nominal central impact on the ASICs.

223 1. The vector of noise hits \mathbf{b} for a given ASIC can be decomposed into

$$\mathbf{b} = \mathbf{u} + c\boldsymbol{\alpha}, \quad (1)$$

224 where \mathbf{u} represents the contribution of the incoherent noise. The vector $\boldsymbol{\alpha}$ characterises
 225 the correlation among the ASICs. More specifically, its components quantify the relative
 226 contributions of the individual channels to the coherent noise. The scalar parameter c
 227 characterises the level of the coherent noise in a given event.

228 2. From this, the noise covariance matrix can be built as

$$B = \sigma^2 \mathbf{1} + \sigma_c^2 \boldsymbol{\alpha} \boldsymbol{\alpha}^T, \quad (2)$$

229 with $\langle u_i u_j \rangle = \sigma^2 \delta_{ij}$ being the incoherent noise squared, $\mathbf{1}$ the unit matrix and σ_c^2 being
 230 the variance of the c -parameter introduced before.

231 3. The vector $\boldsymbol{\alpha}$ is the eigenvector of B with the largest eigenvalue given by $\omega_1 = \sigma^2 + \sigma_c^2$.
 232 In case of only one source of coherent noise, any other eigenvector orthogonal to $\boldsymbol{\alpha}$
 233 should have the eigenvalue σ^2 . In this model, the spectrum of eigenvalues is expected
 234 to be flat except for one eigenvalue from which the coherent noise can be derived. The
 235 Figure 11 shows the spectra of eigenvalues obtained for the four ASICs. The variance
 236 of the coherent noise σ_c^2 of the ASICs can be deduced from the largest eigenvalues
 237 and another one chosen from the flat parts of the spectra, which is reasonably fulfilled
 238 starting from $Rank = 9$. The eigenvalues at that rank are defined as σ^2 . The errors on
 239 the eigenvalues shown in the figure are derived according to the following plausibility
 240 consideration. According to [11] the eigenvalues are bounded by

$$\lambda_n + \sigma^2 b_- \leq \omega_n \leq \lambda_n + \sigma^2 b_+ \quad (3)$$

241 with $b_{\pm} = (1 \pm \sqrt{T/N})^2$ where T is the number of sources, here the ASIC channels,
 242 and N is the number of events. The λ_n are the true variances of the coherent noise
 243 where $\lambda_1 = \sigma_c^2$ in this analysis. The bounds span a range $\sigma^2(b_+ - b_-)$. For one source,
 244 i.e. $T = 1$, this agrees with the statistical error of the variance multiplied by a factor
 245 $\sqrt{2}$. Thus, to obtain the statistical error of the eigenvalues, the range of the bounds is
 246 calculated and divided by $\sqrt{2}$.

247 After these considerations, it can be concluded that the eigenvalues for the two event
 248 types agree within statistical errors, which is particularly true for the largest one which
 249 carries the information on the coherent noise.

250 Figure 12 shows the eigenvectors, normalised to unity, associated with the highest
 251 eigenvalue obtained in the same scan for signal and pedestal events. In some cases the
 252 eigenvectors feature the opposite sign. In that case also the reflected vector is given in
 253 the figure. This sign ambiguity of PCA is reported also in the literature, e.g. [12], and

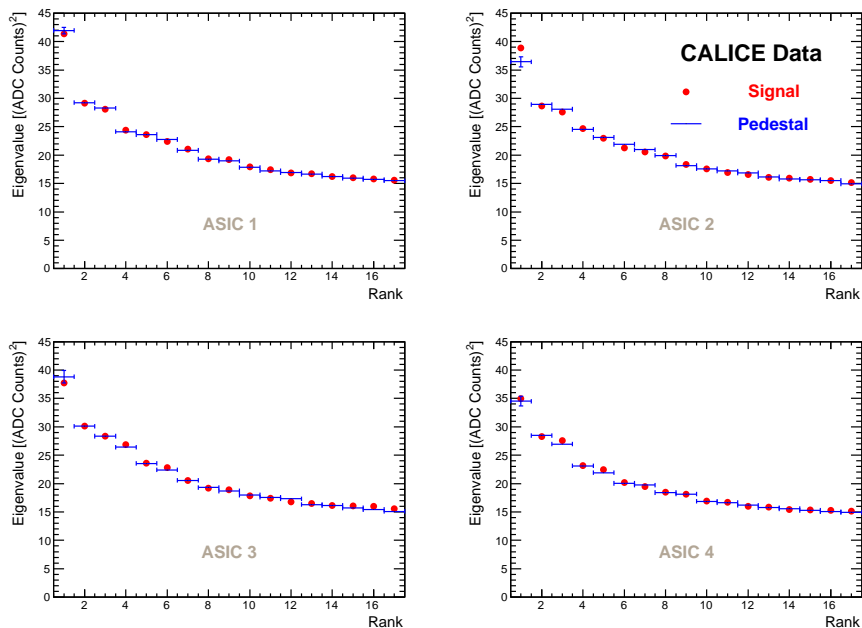


Figure 11: *Eigenvalues as obtained in a Principal Component Analysis of signal and pedestal events for nominal central impact on the ASICs. The eigenvalues are ordered in decreasing order. The statistical error is given for the largest eigenvalue of the pedestal events.*

254 constitutes no hint of an inconsistency. The eigenvectors are thus in good agreement
 255 for signal and pedestal events.

256 A representation of the coherent channel noise can now be achieved by multiplying
 257 the variance, σ_c^2 , with the component squared of the corresponding eigenvalue. The
 258 coherent noise is shown in Figure 13.

259 It is clearly visible that for ASIC 1 and ASIC 3 the coherent noise is concentrated
 260 around the central channel numbers. The source of the coherent noise is not known but
 261 with a value of maximal 5 (ADC counts)², see Figure 13, it is much smaller than the
 262 variance of the incoherent noise of about 20 (ADC counts)², see next step. There is no
 263 evidence that the observed coherent noise is different for signal and pedestal events.

264 4. The incoherent noise per channel can be obtained from the deflated matrix

$$B' = B - \sigma_c^2 \alpha \alpha^T. \quad (4)$$

265 In this matrix the off-diagonal elements are flat around a null value. The diagonal
 266 elements, however, can be interpreted as the channel independent incoherent channel
 267 noise squared. The matrices obtained upon central impact on the ASICs in signal events
 268 are displayed in Figure 14. As expected, they feature dominant diagonal elements.

269 For confirmation, the diagonal elements are displayed separately in Figure 15. As
 270 already mentioned above their values are around 20 (ADC counts)² and channel inde-
 271 pendent.

272 In Section 5 the incoherent channel noise will be employed in the noise simulation of
 273 the ASICs.

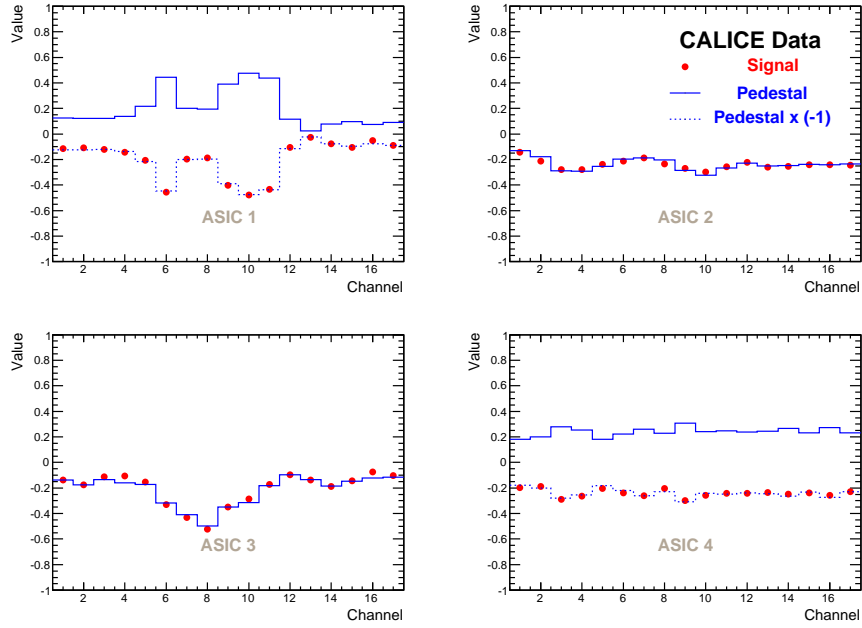


Figure 12: Eigenvectors associated to the largest eigenvalues as obtained in a Principal Component Analysis of signal and pedestal events for nominal central impact on the ASICs. These eigenvectors indicate the location of coherent noise within the ASICs. In case of a sign flip between the eigenvectors for signal and pedestal events, the reflected eigenvector for pedestal events is indicated, too.

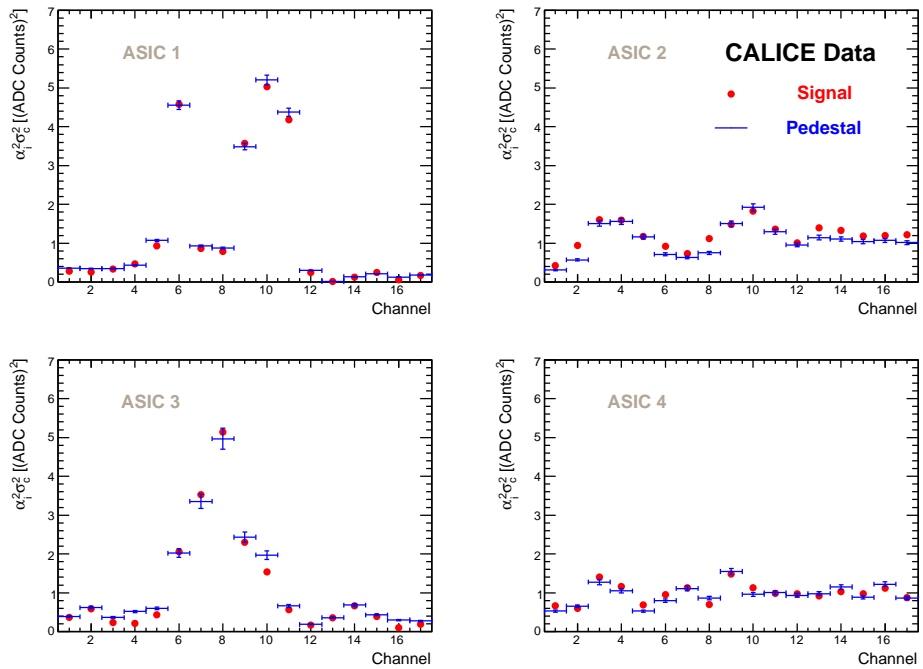


Figure 13: Level of coherent noise in the four ASICs.

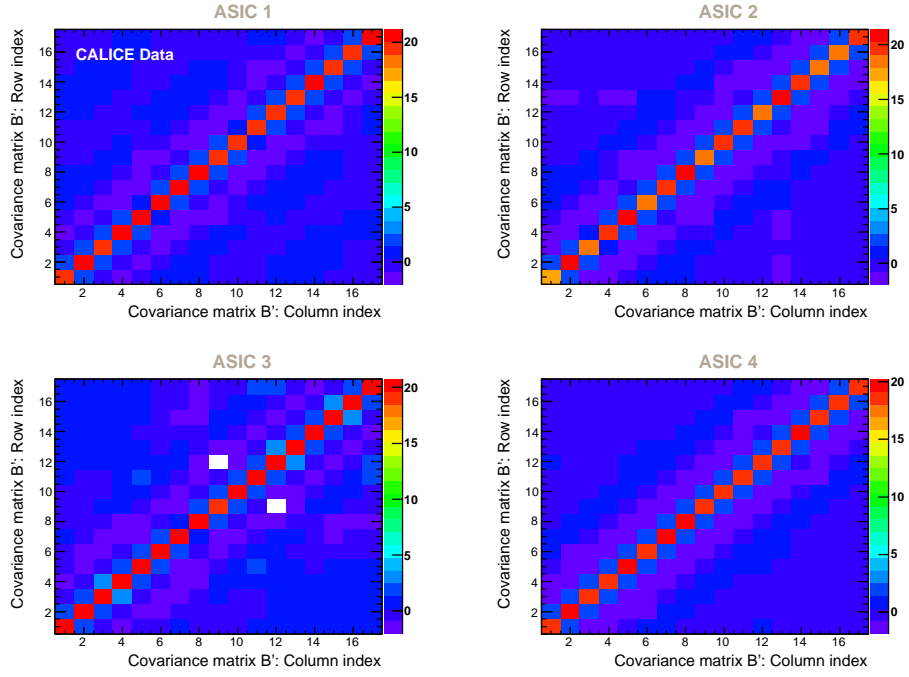


Figure 14: *Deflated matrix B' for the four ASICs as obtained in a Principal Component Analysis for nominal central impact on the ASICs. Here, the matrices are shown for signal events. The colour represents the value of the matrix element in units of $(\text{ADC counts})^2$.*

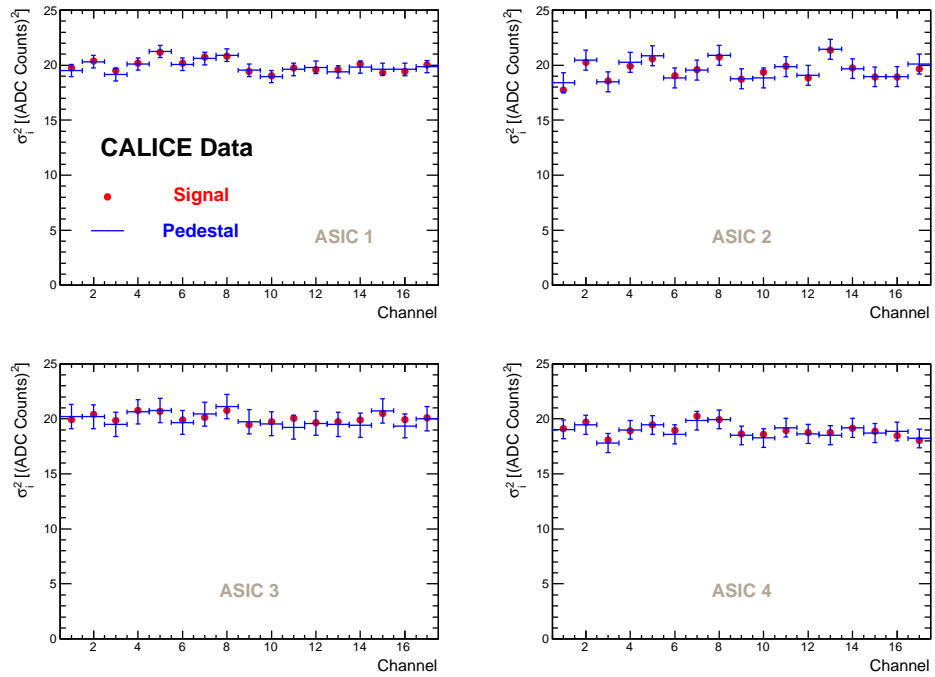


Figure 15: *Level of incoherent noise in the four ASICs.*

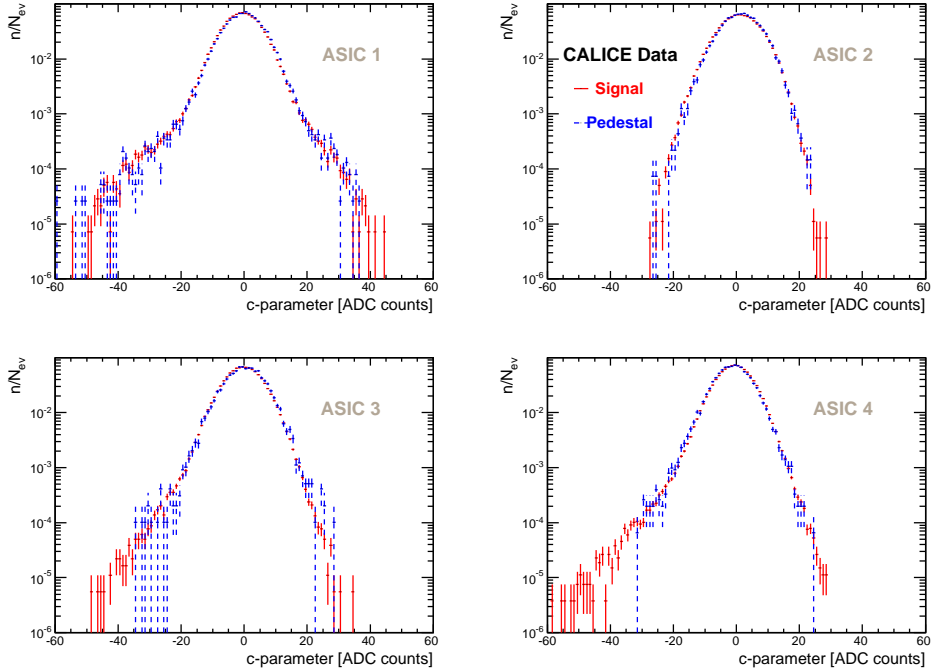


Figure 16: Spectra of the c -parameter as obtained for nominal central impact on the four ASICs for signal and pedestal events. See text for the definition of the c -parameter. The histograms are normalised to unity.

- 274 5. Since all channels of an ASIC can be assumed to be equal, the variance $\sum u_i^2$ reaches a
 275 minimum. Thus, the c -parameter can be estimated by requiring the quantity $\sum (b_i - \alpha_i)^2$
 276 to be minimal. From this it follows that

$$c = \boldsymbol{\alpha} \cdot \mathbf{b}. \quad (5)$$

277 Using this, the coherent noise could be estimated and subtracted on an event-by-event
 278 basis. In this analysis the knowledge of the c -parameter together with other noise
 279 quantities will be exploited to simulate the noise of the ASICs. The c -parameter spectra
 280 for the four ASICs are given in Figure 16.

281 Again the spectra are very similar for signal and pedestal events. Since the statistics
 282 of the signal events are considerably larger than those of the pedestal events, the tails
 283 reach larger values.

284 The PCA allows for the conclusion that the presence of shower particles has no significant
 285 influence on noise pattern of the ASICs. In addition, it indicates that, in a yet more quanti-
 286 tative study, the pedestal events can be used to model the noise pattern in the signal events.
 287 This will be done in the following section.

288 **5 Limits determination**

289 This section is dedicated to the determination of upper limits for having shower-induced fake
 290 hits above a given threshold. As a first result it can be reported that *no signal* above a MIP
 291 is observed in the signal and the pedestal events, such that the upper limit on the probability
 292 that shower particles induce a fake signal at the MIP level can be set to $6.7 \cdot 10^{-7}$ at the 95%
 293 confidence level. This number is derived from the run with the highest statistics listed in
 294 Table 1. In the remainder of this section, this result is extended towards smaller thresholds.
 295 As it is rather expected that the shower induces fake signals towards small ADC counts, the
 296 threshold is varied between 15 and 30 ADC counts, which corresponds to about 1/3 to 2/3
 297 of the signal created by a MIP. This covers the region of noise cuts studied in [8] and allows
 298 for the investigation of the influence of the particle shower towards smallest ADC values.
 299 Values smaller than 15 ADC counts have been discarded as these show a large sensitivity to
 300 the residual pedestal instabilities.

301 **Limits on signals in the presence of background**

302 The comparatively small ADC values require the determination of the upper limits in the
 303 presence of background given by the intrinsic noise of the ASICs. In this case, the Poissonian
 304 probability density function f' for observing n events based on a sample statistics k is given
 305 by [13]:

$$f'(n; \lambda_S + \lambda_B) = f(n; \lambda_S + \lambda_B) / \sum_{n_B=0}^k f(n_B; \lambda_B). \quad (6)$$

306 Here, λ_S and λ_B are the Poissonian parameters for *S*ignal and *B*ackground, respectively. The
 307 probability density function $f(n; \lambda_S + \lambda_B)$ is the sum of the independent Poissonian distribu-
 308 tions for signal and background to the Poissonian parameter $\lambda = \lambda_S + \lambda_B$. The probability
 309 distribution function in the denominator of Equation 6 ensures that f' is normalised to 1 for
 310 background only events. The sum runs over the possible number of background events, n_B ,
 311 up to the sample statistics k . The probability distribution function to the probability density
 312 in Equation 6 reads

$$F'(k; \lambda_S + \lambda_B) = \sum_{n=0}^{k-1} f'(n; \lambda_S + \lambda_B) = P(\ell < k), \quad (7)$$

313 where $P(\ell < k)$ is the probability to observe any number $\ell < k$. The upper limit $\lambda_S^{(up)}$ for
 314 signal events at the confidence level $\beta = 1 - \alpha$ can then be obtained from

$$\alpha = F'(k + 1; \lambda_S^{(up)} + \lambda_B) \quad (8)$$

315 in case the background is known.

316 As there is no indication that the high-energy showers influence the ASIC response, the limits
 317 will be derived for those four measurement points in which the beam was incident on the
 318 nominal centre of one of the ASICs. The background expectation will be obtained from
 319 simulated events.

320 **5.1 Noise simulation**

321 The simulation of the noise starts out from the noise vector given in Equation 1. The
 322 incoherent noise is thus simulated using a Gaussian $G(x_m, \sigma_i)$ with the σ_i of the individual
 323 ASIC-channels read off from the matrices given in Equation 2. The mean x_m of the Gaussian
 324 is given by the mean measured in the pedestal events in a given run. The part covering
 325 the coherent noise is realised by simulating the c -parameter spectrum and by multiplying
 326 this spectrum with the corresponding component α_i of the eigenvector of a given ASIC.
 327 Figure 16 illustrates that the c -parameter spectrum cannot be approximated by a simple
 328 Gaussian. Rather, it is simulated using an adaptive kernel estimation introduced in [14].
 329 Here, the kernel estimation which corresponds to the implementation in the RooFit package
 330 is employed. The formula used to simulate the noise spectrum S'_i for a channel i thus reads

$$S'_i = G(x_m, \sigma_i) + (\text{sign})K(c)\alpha_i. \quad (9)$$

331 The symbol $K(c)$ describes the kernel estimation introduced before. The *sign* is given by the
 332 scalar product of the eigenvectors obtained for the signal events and pedestal events. The first
 333 aim of the simulation is to reproduce the measured pedestal spectra in this paper. Here and
 334 in the following it is ensured that the number of simulated events is at least 2.5 times larger
 335 than the number of measured events. Thus the statistical error of the simulation is smaller
 336 than that of the data. In order to obtain a maximal level of agreement between the simulated
 337 and the measured pedestal spectra, two free parameters are added to the Equation 9 leading
 338 to:

$$S_i = G(x_m - p_m, \sqrt{\sigma_i^2 - p_\sigma}) + (\text{sign})K(c)\alpha_i. \quad (10)$$

339 These free parameters are used to account for residual off-diagonal elements in the matrices
 340 of Equation 2. In addition, they account for imperfections caused by the loss of information
 341 in using only the eigenvector with the largest eigenvalue. The free parameters are tuned
 342 until a minimum χ^2/ndf is obtained upon comparing the spectra of the pedestal events with
 343 the simulated ones. The range of values of the free parameters are $p_m = [-0.33, 0.25]$ and
 344 $p_\sigma = [1.1, 2.0]$. A comparison between the measured pedestal spectrum of ASIC 1 for Scan
 345 1 and measurement point 3 is given in Figure 17. An excellent agreement between data and
 346 simulation is achieved. The resulting χ^2/ndf as a function of the ASIC number for all runs
 347 with central impact on one of the ASICs is shown in Figure 18.

348 Inspired by the work presented in [15], the number of hits in the simulated spectra are subject
 349 to a final correction. For each bin the inverse error function is calculated according to

$$e(\Delta x, \sigma) = \left[1 - \text{erf} \left(\frac{\Delta x}{2\sqrt{2}\sigma_b} \right) \right] \cdot \Delta x. \quad (11)$$

350 Here, Δx is the difference between simulation and pedestal events and σ_b is the statistical
 351 uncertainty of the data in that bin. This correction aims to balance out residual imperfections
 352 of the simulation without being too sensitive to statistical fluctuations appearing in the tails
 353 of the spectra of the pedestal events. After this final correction, the number of hits above a

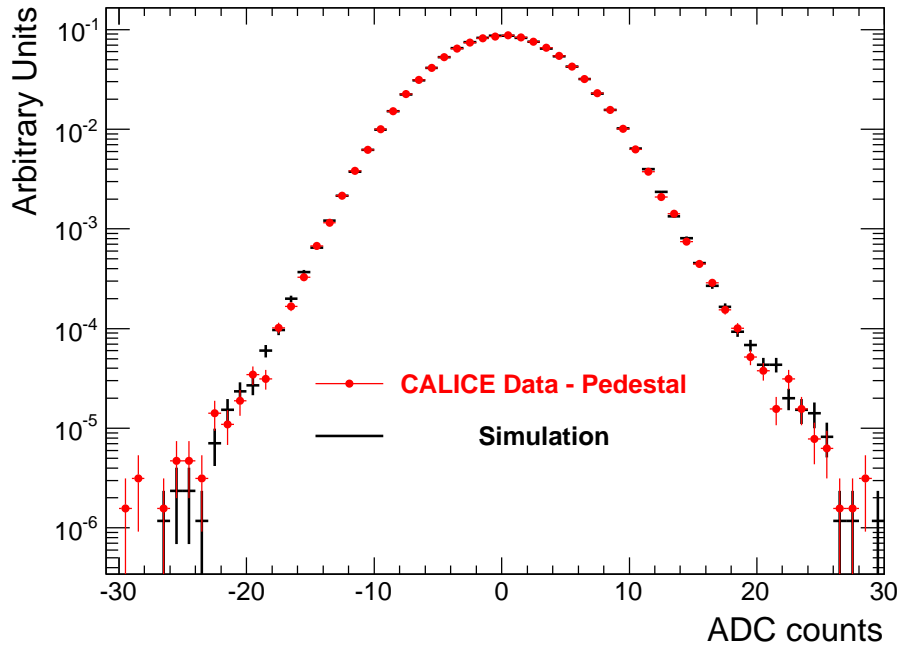


Figure 17: Comparison between the measured and simulated pedestal spectrum at the example of ASIC 1 in Scan 1 and measurement point 3. The details of the simulation are explained in the text.

354 given threshold in pedestal events is compared for data and simulation. The comparisons are
 355 made separately for negative and positive ADC counts and are shown in Figures 19 and 20.
 356 The error on the data is given by the 97.3% confidence interval around the measured number of
 357 hits. Towards large numbers of hits, this corresponds to the 3σ confidence interval. This
 358 interval is chosen since due to the complexity of the noise spectra not all potential effects
 359 are incorporated in the simulation. Systematic uncertainties of the noise modelling can be
 360 estimated from the spread of the simulated distributions of the four ASICs, which should in
 361 principle be identical. Data and simulation agree within the chosen confidence limit where
 362 the agreement is better for negative ADC counts. The agreement achieved validates the
 363 model for making reliable predictions of the expected number of events in signal events.

364 The comparison of the simulated spectra with those measured in the signal events is made in
 365 Figures 21 and 22. Data and simulation are still compatible. For most of the data points the
 366 agreement is within the chosen confidence interval. The deviations may not be attributed
 367 to the actual beam exposure since they occur in their majority for ASICs outside the actual
 368 electromagnetic shower. The agreement is worse towards smaller ADC values while towards
 369 large ADC values data and simulation agree within the chosen limits. The former discussion
 370 indicates that there is no measurable influence of the beam on the ASIC response. Therefore,
 371 in the following the upper limits on the frequency of fake hits are determined.

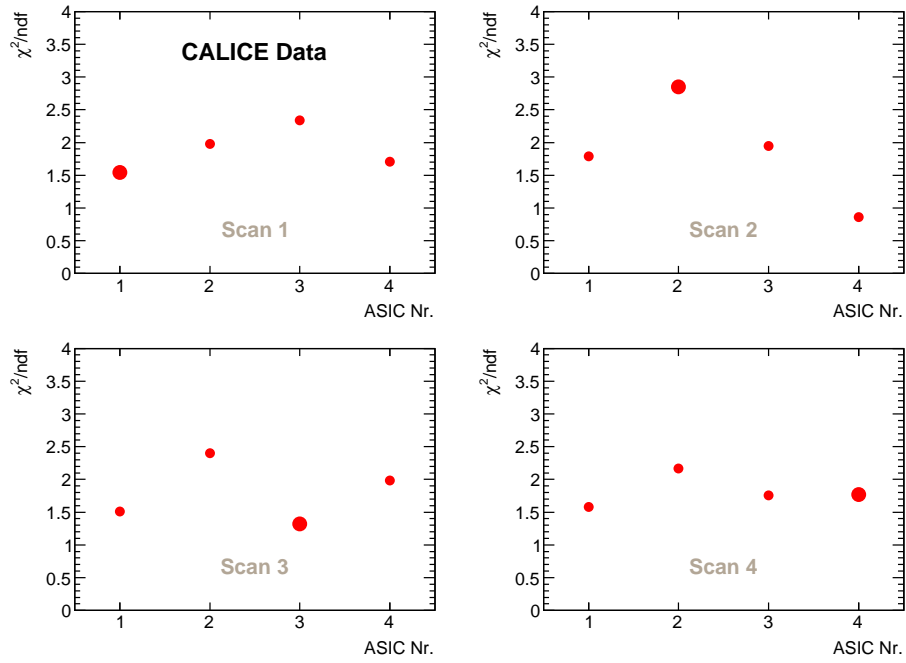


Figure 18: Resulting χ^2/ndf of the comparison between the measured and simulated pedestal spectra. The comparisons are made for the measurement points 3 in the scans, see Table 1. The ASIC which is actually exposed to the beam is indicated by a larger symbol. The ASIC number is given on the x-axis of the graph.

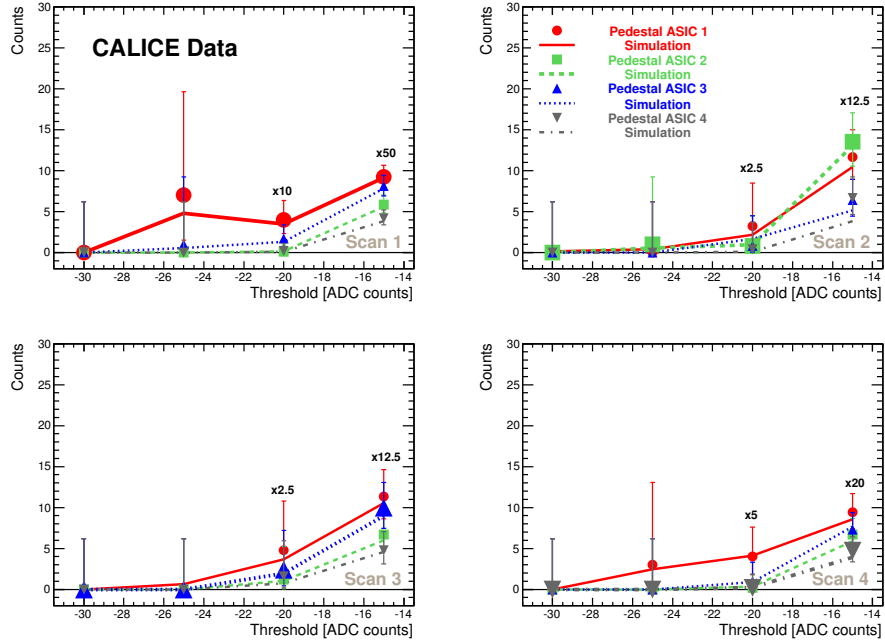


Figure 19: The measured counts below a threshold in pedestal events are compared with those obtained from simulation. The results given in this figure are for negative ADC counts. The error bars on the data points correspond to the 97.3% confidence interval. The comparisons are made for the measurement points 3 in the scans, see Table 1. The ASIC which is exposed to the beam is indicated by a larger symbol. For small absolute thresholds the number of counts have been downscaled by the factors indicated in the figure.

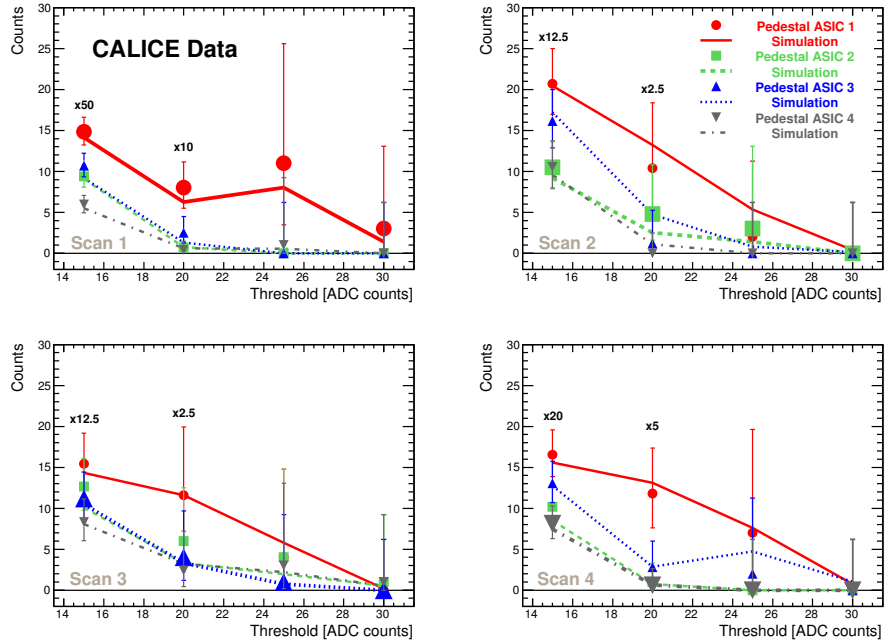


Figure 20: Same as Figure 19 but for positive hits.

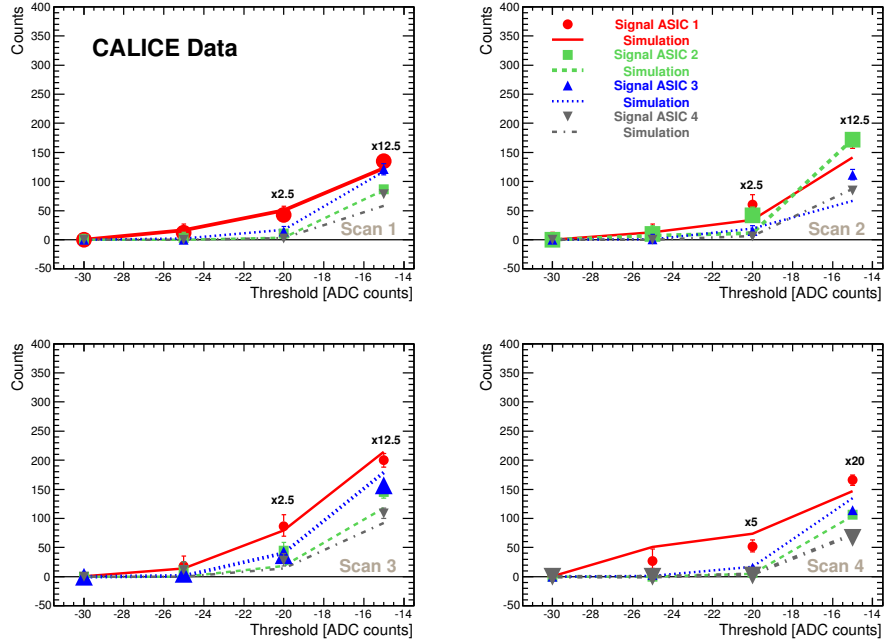


Figure 21: The measured counts below a threshold in signal events are compared with simulation. The results given in this figure are for negative ADC counts. The error bars on the data points correspond to the 97.3% confidence interval. The comparisons are made for the measurement points 3 in the scans, see Table 1. The ASIC that is exposed to the beam is indicated by a larger symbol. For small absolute thresholds the number of counts have been downscaled by the factors indicated in the figure.

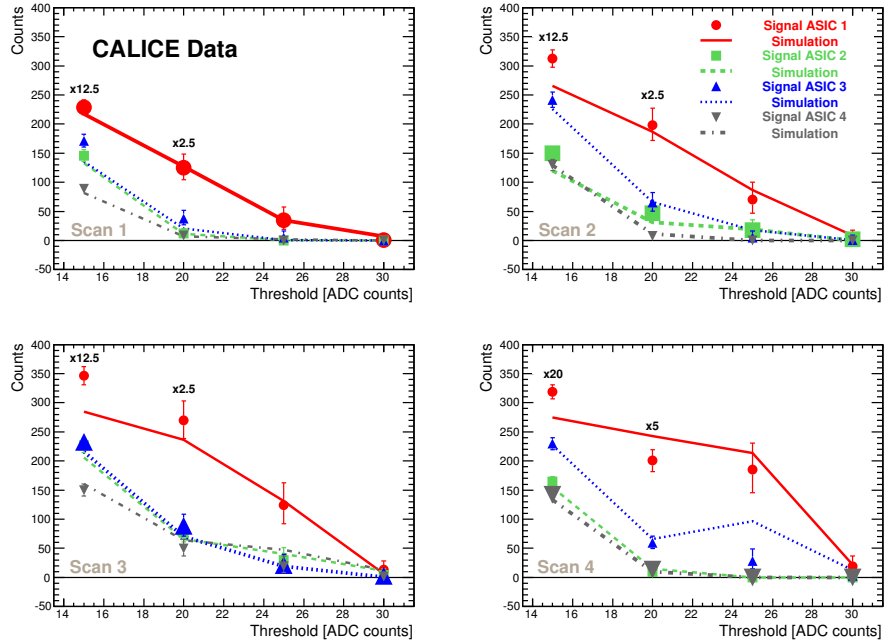


Figure 22: Same as Figure 21 but for positive hits.

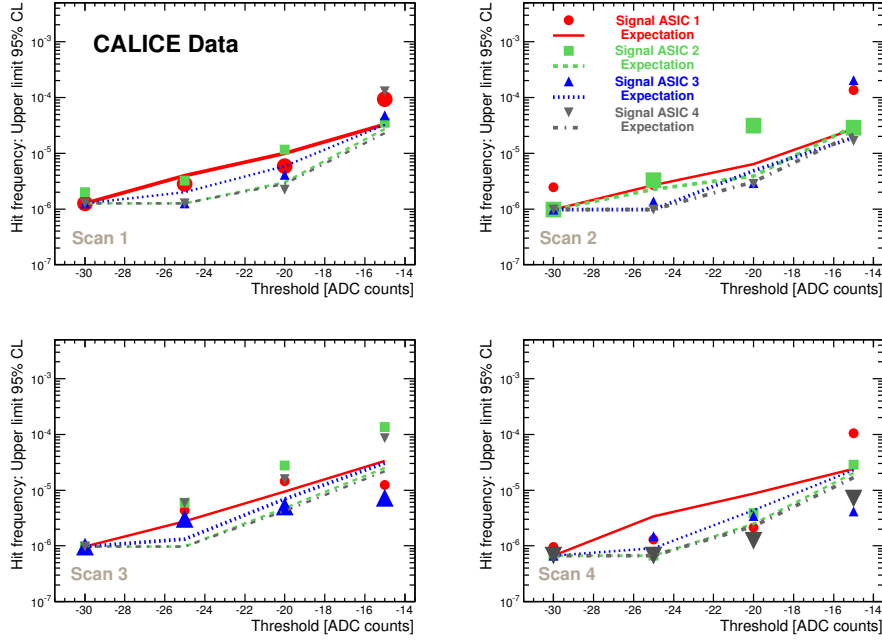


Figure 23: Upper limits on frequencies at the 95% confidence level of fake hits compared with those expected from the pure pedestal events. The limits are given as a function of a threshold for negative values of the ADC counts. The limits are shown for the measurement points 3 in the scans, see Table 1. The ASIC which is exposed to the beam is indicated by a larger symbol.

372 In application of Equations 6, 7 and 8, the sample statistics k is given by the number of
373 hits above a given threshold and λ_B , i.e. the number of expected hits, is obtained from
374 simulation. From this $\lambda_S^{(up)}$ is derived using a computer program available in [13]. Finally,
375 $\lambda_S^{(up)}$ is divided by the total number of hits to calculate the frequency of fake hits. The upper
376 limits at the $\beta = 95\%$ confidence level on the frequency of fake hits are shown in Figures 23
377 and 24 separately for positive and negative ADC counts.

378 For each scan, the upper limits are determined for each of the four ASICs in order to compare
379 the behaviour of an ASIC exposed to the electron showers with those not exposed to the
380 showers. It may be seen that the determined upper limits are always smaller than $5 \cdot 10^{-4}$
381 for the smallest threshold value and smaller than 10^{-5} for the highest threshold value. The
382 observed dependency on the threshold is the same whether or not the ASICs are exposed
383 to the particle showers. The upper limits are compared with sensitivity limits, full lines in
384 Figures 23 and 24, obtained when the frequencies observed in data are replaced by those
385 expected from the simulation. In particular towards large threshold values the derived limits
386 agree well with the expectation. Deviations from the expectation are observed both for ASICs
387 exposed to showers and for those outside the showers.

388 This observation renders it unlikely that there is an influence of the beam on the measured
389 signal. This is in particular true for threshold values relevant for physics analysis in which
390 typically values below 25 ADC counts are discarded. Remaining deviations towards small

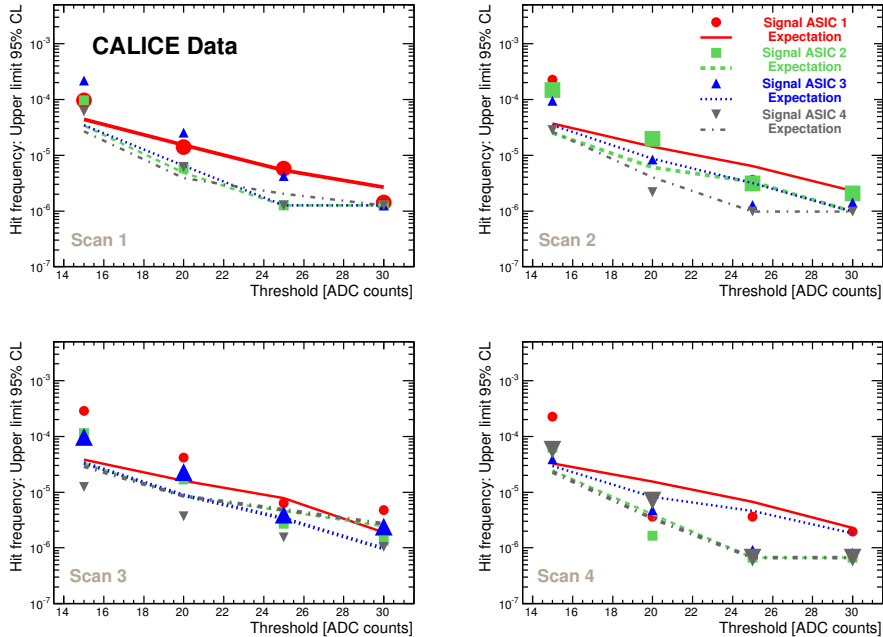


Figure 24: Same as Figure 23 but for positive hits.

391 thresholds from the expectation can be attributed to the influence by other parts of the
 392 experimental set-up which are present when there is a large activity in the detector. These
 393 interspersed signals are not taken into account in the simulation.

394 6 Conclusion and outlook

395 A series of test runs has been performed and analysed in order to prove the feasibility of
 396 having embedded readout electronics for a calorimeter proposed for a future lepton collider.
 397 A detailed analysis of noise spectra of the ASICs exposed to high-energy electron beams has
 398 revealed no evidence that the noise pattern is altered under the influence of the electromag-
 399 netic showers. The probability to have fake signals above the MIP level is estimated to be
 400 smaller than $6.7 \cdot 10^{-7}$. The probability for a fake signal is less than 10^{-5} for a threshold of
 401 $2/3$ of a MIP. For an event of the type $e^+e^- \rightarrow t\bar{t}$ at $\sqrt{s} = 500$ GeV at the lepton collider
 402 about 2500 cells of dimension 1×1 cm² are expected to carry a signal above noise level which
 403 is typically defined to be (60-70)% of a MIP. The results presented in this article have re-
 404 vealed no problems for the design of embedded readout electronics for a detector for a lepton
 405 collider. It is furthermore unlikely that the residual deviations between the observed number
 406 of hits and those expected from normal noise fluctuations can be attributed to the influence
 407 of the beam but rather to an imperfect modelling of the noise spectra for signal events. In
 408 this sense, the presented results constitute a conservative upper limit.

409 Currently, the CALICE collaboration is about to construct a technological prototype [16].
 410 In contrast to the physics prototype, this technological prototype will have the readout elec-
 411 tronics embedded by design. The ASICs employed therein are a straightforward further de-

412 velopment of those of the physics prototype [7] as described in this paper. The technological
413 prototype in general and the ASICs in particular are close to the design currently envisaged
414 for the International Linear Collider which is currently the most advanced proposal for a
415 future lepton collider. A series of tests as described in this article will have to be repeated for
416 this prototype as the electronics are more challenging than the one employed in the physics
417 prototype with respect to compactness and requirements of power saving. Upon repetition of
418 the test a considerably larger amount of interleaved pedestal events will have to be recorded.
419 Future tests should also be conducted with heavily ionising particles up to the point at which
420 radiation effects become apparent. With cross talk effects further reduced, such a research
421 program will allow for the establishment of a complete picture of the feasibility of embedded
422 electronics in radiation environments.

423 **Acknowledgements**

424 We would like to thank the technicians and the engineers who contributed to the design and
425 construction of the prototypes. CALICE conducts test beams at CERN, DESY and FNAL
426 and we gratefully acknowledge the managements of these laboratories for their support and
427 hospitality, and their accelerator staff for the reliable and efficient beam operation. We would
428 like to thank the HEP group of the University of Tsukuba for the loan of drift chambers for the
429 DESY test beam. This work was supported within the 'Quarks and Leptons' programme of
430 the CNRS/IN2P3, France; by the Bundesministerium für Bildung und Forschung, Germany;
431 by the the DFG cluster of excellence 'Origin and Structure of the Universe' of Germany; by
432 the Helmholtz-Nachwuchsgruppen grant VH-NG-206; by the BMBF, grant no. 05HS6VH1;
433 by the Alexander von Humboldt Foundation (Research Award IV, RUS1066839 GSA); by
434 MICINN and CPAN, Spain; by the US Department of Energy and the US National Science
435 Foundation; by the Ministry of Education, Youth and Sports of the Czech Republic under
436 the projects AV0 Z3407391, AV0 Z10100502, LC527 and LA09042 and by the Grant Agency
437 of the Czech Republic under the project 202/05/0653; and by the Science and Technology
438 Facilities Council, UK.

439 Appendix - Mean and RMS of signal and pedestal events

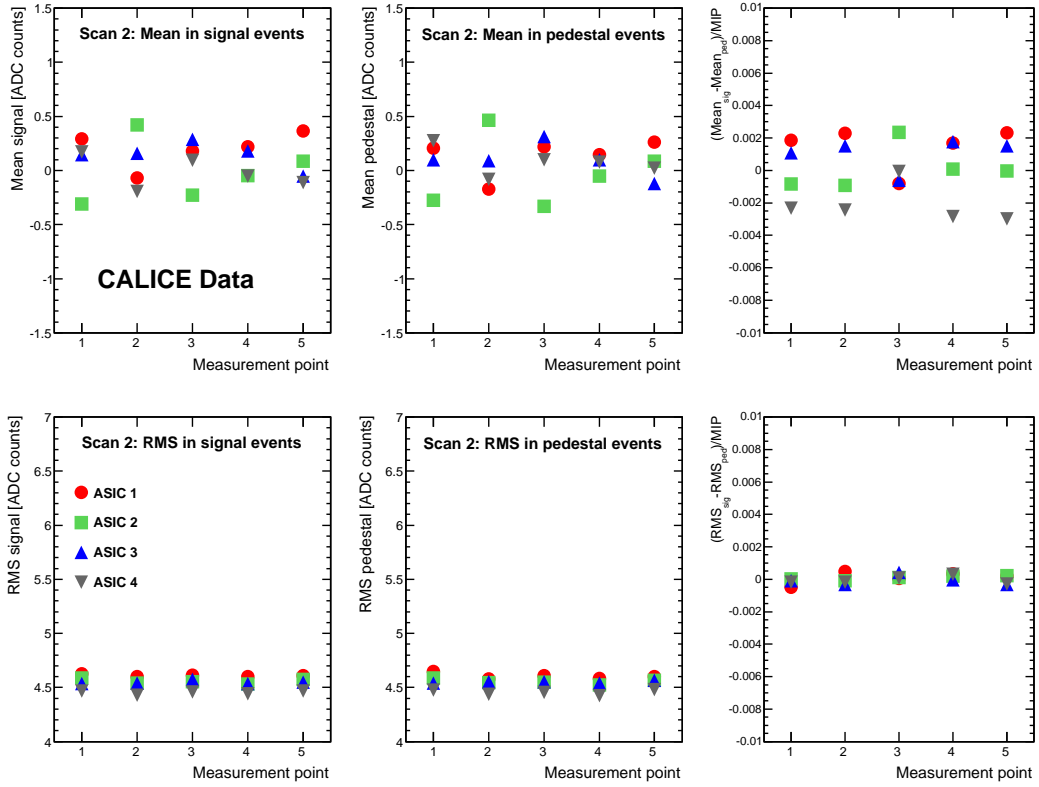


Figure 25: Mean and RMS for signal events and pedestal events. The very right part shows the corresponding differences normalised to the value of a MIP assumed to be 45 ADC counts. The figure displays the result for Scan 2 in which ASIC 2 is scanned. As a cross-check the results for all ASICs are shown.

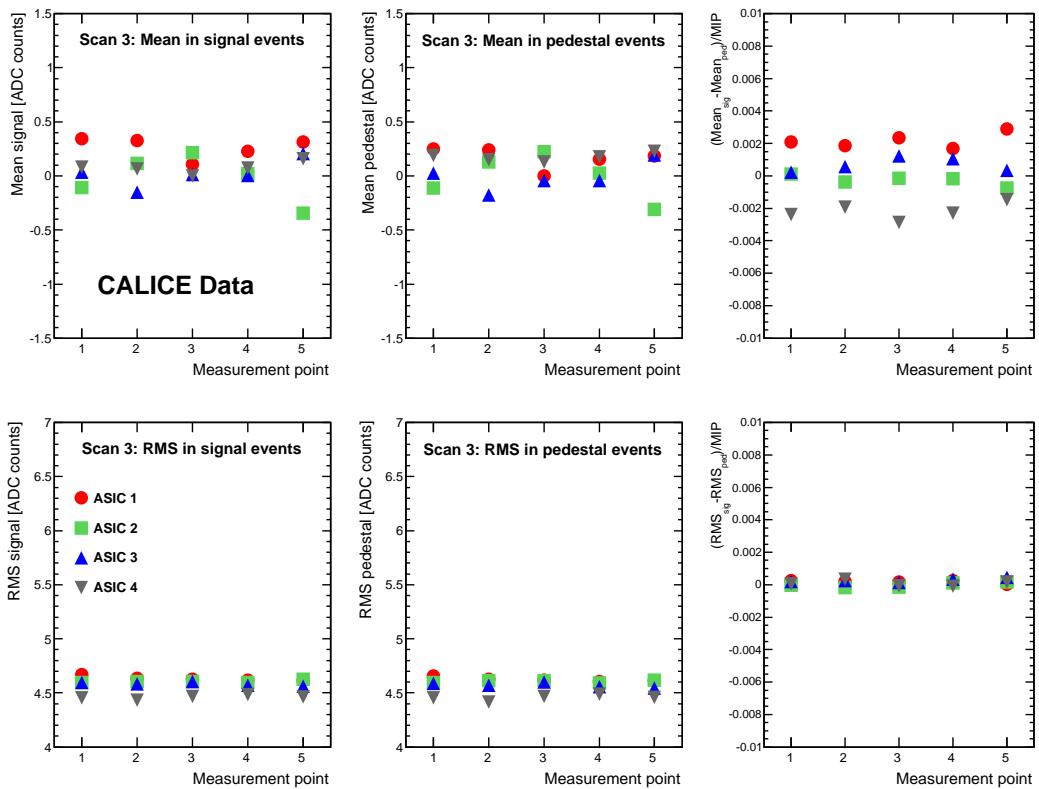


Figure 26: Mean and RMS for signal events and pedestal events. The very right part shows the corresponding differences normalised to the value of a MIP assumed to be 45 ADC counts. The figure displays the result for Scan 3 in which ASIC 3 is scanned. As a cross-check the results for all ASICs are shown.

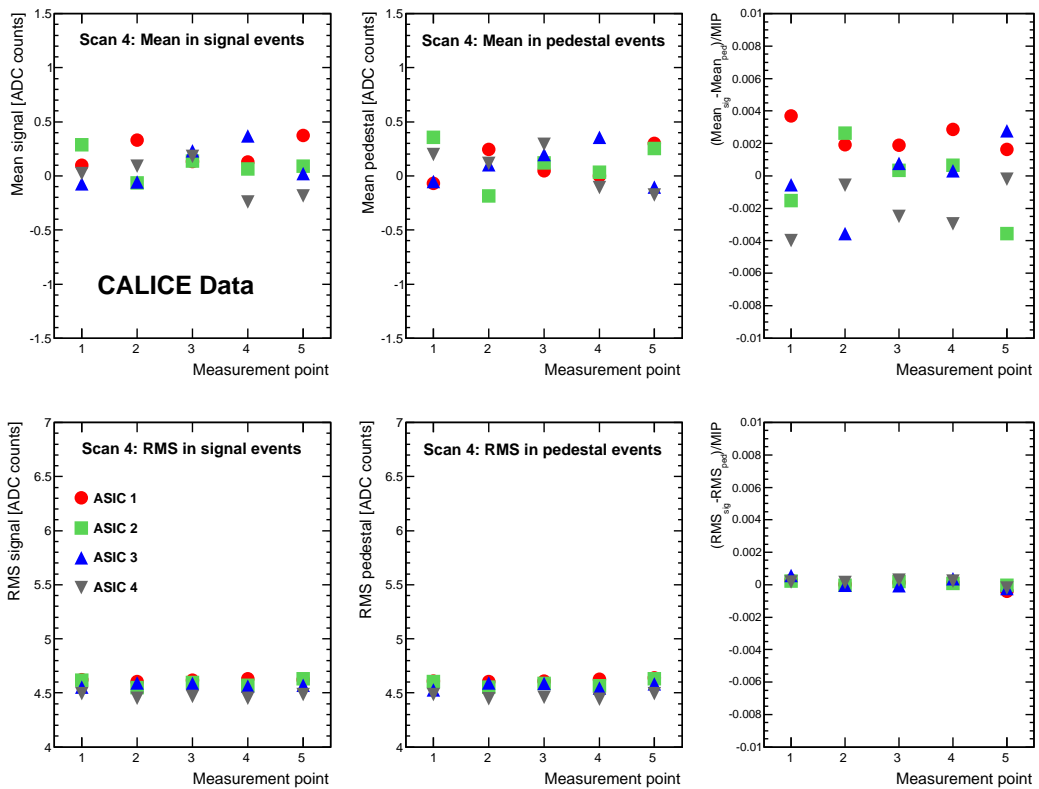


Figure 27: Mean and RMS for signal events and pedestal events. The very right part shows the corresponding differences normalised to the value of a MIP assumed to be 45 ADC counts. The figure displays the result for Scan 4 in which ASIC 4 is scanned. As a cross-check the results for all ASICs are shown.

References

- 441 [1] The ILD Concept Group.
442 *The International Large Detector - Letter of Intent*.
443 DESY 2009-87, Fermilab-Pub-09-682-E, KEK Report 2009-6, arXiv:1006.3396v1 [hep-ex].
- 444 [2] SiD Concept Group, H. Aihara *et al.*
445 *SiD Letter of Intent*.
446 arXiv:0911.0006 [physics.ins-det].
- 447 [3] A. Mazzacane.
448 *The 4th Concept Detector for the ILC*.
449 NIM A **617** 173 (2010).
450 See the full text under: <http://www.4thconcept.org/4LoI.pdf>.
- 451 [4] A. Holmes-Siedle and L. Adams.
452 *Handbook of Radiation Effects*.
453 Oxford University Press, 1993, ISBN 0-19-856347-7.
- 454 [5] I. Laktineh.
455 *CALICE Results and Future Plans*.
456 Presentation at the International Conference on High Energy Physics 2010, ICHEP2010. To appear in
457 the proceedings.
- 458 [6] CALICE Collaboration J. Repond *et al.*
459 *Design and electronics commissioning of the physics Prototype of a Si-W electromagnetic calorimeter for*
460 *the International Linear Collider*.
461 JINST **3** P08001 (2008), arXiv:0805.4833v2 [physics.ins-det].
- 462 [7] C. de la Taille.
463 *Front End Electronics in Calorimetry: From LHC to ILC*.
464 Mémoire d'habilitation à encadrer des recherches, LAL-09-117.
- 465 [8] CALICE Collaboration, J. Repond *et al.*
466 *Response of the CALICE Si-W electromagnetic calorimeter physics prototype to electrons*.
467 Nucl. Instr. and Methods A **608** 372 (2009), arXiv:0811.2354v1 [physics.ins-det].
- 468 [9] CALICE Collaboration, C. Adloff *et al.*
469 *Study of the interactions of pions in the CALICE silicon-tungsten calorimeter prototype*.
470 JINST **5** P05007 (2010), arXiv:1004.4996 [physics.ins-det].
- 471 [10] R. Zitoun.
472 *Study of Noise in the November 1998 barrel run*.
473 ATL-LARG-99-006.
- 474 [11] R. Everson and S. Roberts.
475 *Inferring the Eigenvalues of Covariance Matrices from Limited, Noisy Data*.
476 IEEE Transactions on Signal Processing Vol.48, No. 7, 2083 (2000).
- 477 [12] R. Bro, E. Acar and T.G. Kolda.
478 *Resolving the sign ambiguity in the singular value decomposition*.
479 Journal of Chemometrics, Volume **22**, Issue 3, 135 (2007).
- 480 [13] S. Brandt.
481 Datenanalyse.
482 BI-Wiss.-Verl., 1992, ISBN 3-411-03200.
- 483 [14] K.S. Cranmer.
484 *Kernel Estimation in High-Energy Physics*.
485 Comput.Phys.Commun. **136** 198 (2001), arXiv:hep-ex/0011057v1.
- 486 [15] B. Malaescu.
487 *Mesures précises de sections efficaces $e^+e^- \rightarrow$ Hadrons: tests du Modèle Standard et applications en*
488 *QCD*.
489 Thèse doctorale, LAL-10-113.
- 490 [16] R. Pöschl.
491 *A large scale prototype for an SiW electromagnetic calorimeter for the ILC - EUDET module*.
492 Nucl. Instr. and Meth. A **617** 113 (2010).